Digest Journal of Nanomaterials and Biostructures Vol. 6, No 2, April - June 2011, p. 609 - 624

INFLUENCE OF ANNEALING TREATMENT OF NANO-HYDROXYAPATITE BIOCERAMICS ON THE VIBRATIONAL PROPERTIES

C. S. CIOBANU[a,b], E. ANDRONESCU[a], A. STOICU[b], O. FLOREA[b], P. LE COUSTUMER[c], S. GALAUP[d], A.DJOUADI[e], J.Y. MEVELLEC[e], I. MUSA[e], F. MASSUYEAU[e], A. M. PRODAN[a,f,g], KHALID LAFDI[h], R. TRUSCA[i], I. PASUK[b], D. PREDOI[b*]
[a]*University Politehnica of Bucharest, Faculty of Applied Chemistry and Materials Science, Department of Science and Engineering of Oxide Materials and Nanomaterials, 1-7 Polizu Street, P.O. Box 12-134, 011061 Bucharest, Romania*
[b]*National Institute of Materials Physics, P.O. Box. MG 07, 077125, Magurele, Romania*
[c]*Universite Bordeaux 1, Avenue des Facultés, Bat 18, 33405 Talence Cedex France*
[d]*IUT Michel de Montaigne –Bordeaux 3, 1 rue Jacques Ellul 33080 Bordeaux cedex France*
[e]*Institut des Matériaux-Jean Rouxel, 02 rue de la Houssinière BP 32 229, 44 322 Nantes, France*
[f]*Emergency Hospital Floreasca, Bucharest 5, Calea Floresca nr 8, sector 1, Bucarest, Romania*
[g]*Carol Davila University of Medicine and Pharmacy, 8 Eroii Sanitari, sector 5, Bucharest, Romania*
[h]*University of Dayton, 300 College Park, Dayton, Ohio 45469, USA*
[i]*METAV Research & Development, 31 C.A. Rosetti, sector 2, Bucharest, Romania*

Nano-hydroxyapatite bio-ceramics were synthesized by sol-gel method. The gel was dried at 80°C for 96 h. The dried gels were individually heated at a rate of 5^0C/min up to 600^0C, 800^0C, and 1000^0C. X-ray diffraction (XRD), transmission electron microscopy (TEM) and scanning electron microscopy (SEM) were used for to characterize the composition, morphology and particle size of samples. At 800°C a small amount of CaO (about 0.3 wt%) was detected in which increased after annealing at 1000°C (about 1.1 wt%). The crystallites are elongated along the *c* crystallographic axis, but the size anisotropy decreases with increasing temperature above 800°C. The size along the elongation axis increased from 43 nm at 80°C to about 143 nm at 1000°C, as determined by XRD, and from 120 to 280 nm, as measured by TEM. The functional groups were analyzed using Fourier transform infrared (FTIR) and Raman spectroscopies confirming the presence of various PO_4^{3-} and OH^- bands in the samples. After calcination at 1000^0C the bands are more intense which indicates an increase in the cristallynity. The photoluminescence (PL) of HAp treated at various temperatures (80, 600, 800, 1000 °C) was also studied. hFOB 1.19 osteoblats cells were used to determine cell proliferation, viability and citotoxicity after interaction with the prepared bioceramics. To evaluate cell proliferation rate quantitative by the hFOB 1.19 cells on HAp samples were cultured to 4 days. Cellular morphology was investigated using FESEM to obtain qualitative information of osteoblast cells on HAp samples. The number of hFOB 1.19 cells on control HAp_80, HAp_600, HAp_800 and HAp_1000 was 400±30, 360±25, 350±21, 320±16 and 300±10 after 4 days. Our results proved that the HAp sintered at 1000^0C promoted osteoblast cell attachment and adhesion.

(Received February 25, 2011; accepted March 14, 2011)

Keywords: Hydroxyapatite, Nanoparticle, Vibrational spectroscopies, Time-resolved Photoluminescence, Osteoblasts cells

---

[*] Corresponding author: dpredoi68@gmail.com

1. Introduction

In the last years, considerable attention has been given to the composites which would remain in place after implantation and provide an agent which would encourage osteogenesis [1]. Nanotechnology has been applied in the field of biomaterials to improve the biological responses of synthetic hydroxyapatite (HAp) with is more close to mineral nano-grade HAp in bone [2]. Nano-HAp exhibits certain superiority in the field of orthopedic implants for its improved biological and biomechanical properties [3]. Development of HAp based biocomposite materials could be one way to overcome the poor mechanical properties of dense HAp. Hydroxyapatite is an important substitute material in orthopedics and dentistry due to the chemical and biological similarity of this material to the mineral constituent of human bone [4]. The control of morphology and mean size of powders is important in the applications of HAp. It is well known that not only the morphology and mean size of the powders but also the stoichiometry and purity of the powders affect the properties of the HAp in many applications fields such as orthopedic and dental field as a paste, granules, or porous blocks for implants [5].

Hydroxyapathite is used in bio-medical applications due to its bio-compatibility with bone structure. Used as coating for some protease this improves the healing duration and the quality of the body acceptance. Considerable efforts were made to improve the mechanical properties of HAp by altering both materials composition and their crystallinity using macro and nanotechnology approaches [6-19]. Studies were carried out to produce synthetic nano-HAp materials [6]. Nanosized HAp powders exhibit better bioactivity and improves dentification properties than coarser crystals [7-8]. HAp can be crystallized from solution but also synthetisized in the solid state at high temperature [9-12].

Various techniques have been used for prepare the hydroxyapatite (HAp). HAp can be prepared by several synthetic routes which include hydrothermal synthesis [13] sol-gel processes [14], and direct precipitation from aqueous solutions [15]. Sol-gel is a wet chemical method which offers a molecular mixing of calcium and phosphorus which improved the chemical homogeneity of the resulting materials. The high reactivity of the sol-gel powders seems to reduce processing sintering temperature [16].

In addition to HAp materials composition and properties, HAp response to cell environment is crucial. In general, the surface properties of biomaterials are associated with cell adhesion and subsequent various cell behaviors such as proliferations, migration, cytoskeletal arrangement, and apoptosis [17]. Cell adhesion and its performance depend on the characteristics of substrates including chemical composition, surface charge, water wettability, roughness and size of cytophilic area [17]. Since HAp is composed of calcium phosphate based ceramics, it will play a significant role in the substitution and reorganization of hard tissue.

The present paper uses the sol-gel method to synthesise hydroxyapatite (HAp), the physical-chemical properties and biocompatibility of HAp before and after calcinations at 600, 800 and 1000^0C was studied. The effect of heat treatment on Ca/P ratio and phase content, grain and crystallite size of the samples were investigated by X-ray diffraction (XRD). For further support of the XRD analysis, we used TEM to observe the structure of the samples. The morphology of the samples was investigated by transmission electron microscopy (TEM) and scanning electron microscopy (SEM). The functional groups of the powders were analyzed using Fourier transform infrared spectroscopy (FTIR) and Raman spectroscopy. The powders were also characterized by time-resolved photoluminescence.

The biocompatibility of HAp samples before and after calcination at 600, 800 and 1000°C, was assessed by cell proliferation assay and morphology studies.

2. Experimental

2.1. Powder preparation

The HAp ceramic powder was prepared (Ca/P molar ratio: 1.67) using Ca $(NO_3)_2{\cdot}4H_2O$ and P_2O_5 by a simple sol-gel approach. A designed amount of phosphoric pentoxide (P_2O_5, Merck) was dissolved in absolute ethanol to form a 0.5 mol/l solution. A designed amount of calcium nitrate tetrahydrate was also dissolved in absolute ethanol to form a 1.67 mol/l solution [20-21]. The mixture was stirred constantly for 24 h by a mechanical stirrer, allowing the reaction to complete at 80^0C. A transparent gel was obtained. The gel was dried at 80^0C for 96 h (HAp_80) in an electrical air oven. The dried gels were individually heat treated at the rate of 5^0C/min up to 600^0C (HAp_600), 800^0C (HAp_800) and 1000^0C (HAp_1000) for 6h. The sintered powders were ball milled at 100 rpm to produce fine powders.

2.2 Powder characterization

X-ray diffraction (XRD). The samples were characterized for qualitative and quantitative phase content by X-ray diffraction by using a Bruker D8-Advance X-ray diffractometer, in powder setting, equipped with copper target X-ray tub, Ni filter, and a high efficiency linear detector of Lynx Eye type. The patterns were scanned in the 2θ range 15 – 140^o, with a step size of 0.02^o and 8 s per step.

Scanning electron microscopy (SEM-EDS).The elemental analysis and morphology of the samples were characterized using a FESEM HITACHI 4700 coupled with an energy dispersive X-ray attachment (EDAX/2001 device).

Transmission electron microscopy (TEM) studies were carried out using Technai 120kev from FEI to precise the evolution of HAp with the thermal treatment. Classic modes such bright field (BF) to image the texture of the materials (shape, dimension) and Selected Area Diffraction (SAD) to precise the structure (crystallographic parameters) were used. The samples were prepared using ultramicrotomy to obtain thin samples with a thickness inferior to 80 nm. The preparations were deposited on a copper grid covered by a thin film of amorphous carbon. This protocol has been used in order to minimize sample artefacts such amorphization or preferential ablation induced by FIB for example or by ionic ablation.

FT-IR spectroscopy. The functional groups present in the prepared powder and in the powders calcined at different temperatures were identified by FTIR (Spectrum BX Spectrometer). For this 1% of the powder was mixed and ground with 99% KBr. Tablets of 10 mm diameter for FTIR measurements were prepared by pressing the powder mixture at a load of 5 tons for 2 min and the spectrum was taken in the range of 400 to 4000 cm^{-1} with resolution 4 and 128 times scanning.

Raman Spectroscopy. Micro-Raman spectra on HAp powders were performed in a backscattering geometry at room temperature and in ambient air, under laser excitation wavelength 514 nm, using a Jobin Yvon T64000 Raman spectrophotometer under a microscope.

Time-resolved photoluminescence (PL). Ultrafast PL experiments were carried out with a regenerative amplified femtosecond laser system (Spectra Physics Hurricane X) delivering 100 fs pulses at 1 kHz, 800 nm, and 1 W mean power. Composite samples were excited at 267 nm by triple harmonic generation. Transient signals were spectrally dispersed into an imaging spectrograph. The time-resolved emission spectra were detected with a streak camera of temporal resolution < 20 ps.

Cell culture. The hFOB 1.19 osteoblasts cells line was purchased from ATCC (American Type Culture Collection) and maintained in DMEM, containing 3,7 g/L sodium bicarbonate,4,5g/L D-glucose, 4,7g/L HEPES, 4 mM L-glutamine, 0,1 mM sodium pyruvate, 100 U/ml penicillin, 100 U/ml streptomycin and 10% (v/v) fetal bovine serum. Cells were grown in 5% CO_2 at 37^oC and plated at 5x104cells/cm^2 in Ø 100 mm culture dishes with a medium change twice a week. When 70-80% confluence was reached, cells were passaged and hFOB 1.19 cells prior to passage 4 were used in this study.

The HAp ceramic discs with dimensions of 10 mm Ø x 10 mm were rinsed in distilled water and autoclaved at 125°C/0.14 MPa for 60 min.

Cells cultured in dishes prior to passage 3 were detached by treatment with trypsin-EDTA (0.25% and 0.03% respectively) and loaded on HAp ceramic discs at a seeding density of 5x104cells/cm^2 in 24-well plates. Cells cultured in 24-well plates at the same seeding density were used as control.

Cell proliferation assay. To evaluate cell proliferation rate quantitative by the hFOB 1.19 cells on HAp samples were cultured for up to 4 days. Ten different fields per sample were randomly chosen under a microscope and normal cells were counted by two observers at days 1, 2 and 4, respectively.

FESEM examination. After 5 days'incubation on HAp sample, hFOB 1.19 cells were fixed in 2,5% glutaraldehyde, treated with 1% osmium tetroxide and dehydrated. The samples were then subjected to critical point drying and coated with gold-palladium. The cell morphology was determined by FESEM.

Morphology. The cells were plated at day one at a density of $5x10^4$cells/cm^{2}on the ceramics discs. At specific time points cells were imaged by a bright field inverted microscope (Olympus IX7). Images were acquired by specific software Cell F using a CCD video camera COLORVIEW. The cells were grown on the specimens for 24 h, treated with 1µM hypericin and analyzed by fluorimetric microscopy.

3. Results and discussion

The effect of the post-treatment temperature on the morphologies and crystal structures of the powders were investigated by SEM and TEM. Figure 1 shows the XRD patterns of the HAp powders. After heat treatment at 600°C the pattern did not change. After being calcined at 800°C, the HAp peaks sharpened and a weak peak of calcium oxide (CaO) appeared. The concentration of calcium oxide increases after heat treatment at 1000°C. This can be due to the chemical decomposition of the remaining calcium nitrate as follows [22]:

$$Ca(NO_3)_2 \rightarrow Ca(NO_2)_2 + (1/2)\ O_2$$
$$Ca(NO_2)_2 \rightarrow (1/3)Ca(NO_3)_2 + (2/3)CaO + (4/3)NO$$
$$Ca(NO_3)_2 \rightarrow CaO + 2NO_2 + (1/2)O_2$$

The presence of CaO after heat treatment is in agreement with the results reported earlier by Kutty [23] and Skinner et al [24]. With the increase of the calcination temperature HAp would have started losing hydroxyl groups forming various phosphates. The microstructure of the ceramic powders prepared by sol-gel synthesis is strongly affected by the sintering temperature [25]. The proposed reaction is [26]:

$$Ca_{10}(PO_4)_6(OH)_2 \xrightarrow{\qquad\qquad} 3Ca_3(PO_4)_2 + CaO + H_2O$$

The tricalcium phosphate phase was not detected by XRD. The crystal symmetry of this phase is lower (the alpha phase is monoclinic and the beta phase is hexagonal), hence the diffracted intensity is distributed in more much lines and correspondingly weaker than in case of CaO, with cubic structure.

The determination of the average crystallite size (that is of perfectly ordered crystalline domains) by XRD methods is based on the Scherer formula:

$$D = \lambda/B \cos\theta$$

where D is the averaged length taken in the direction normal to the lattice plane that corresponds to the diffraction line at the Bragg angle θ, B is the broadening of this line due to the small crystallite size (integral breadth) and λ is the wavelength of X-rays.

Another source of line broadening is the local distortion of the lattice (microstrain), which can be expressed as the root mean square of the relative variation of the interplanar spacings (*d*):

$$\text{Microstrain} = \langle \varepsilon^2 \rangle^{1/2}$$

where $\varepsilon = \Delta d/d$. The size and strain contributions to the broadening are usually not easy to be separated, but the analysis is facilitated by using specialized codes available nowadays for diffraction data processing.

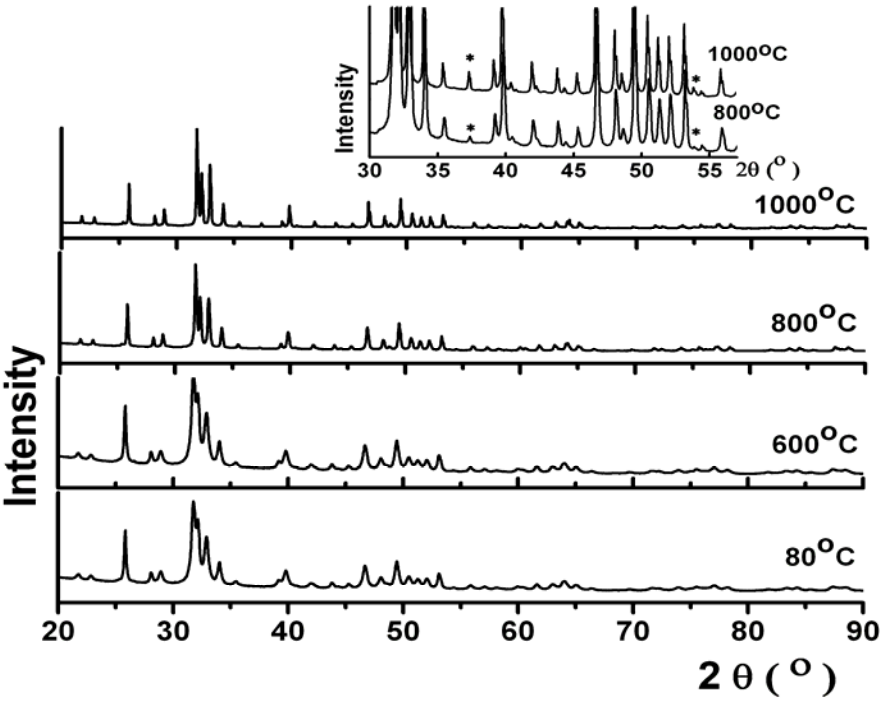

Fig. 1. The X-ray diffraction patterns of the powder after heat treatment at 80°C, 600°C, 800°C and 1000°C (= CaO)*

Within this study the XRD data were processed by the MAUD v. 2.26 software [27], aiming to determine the percentage of lime, and the average crystallite size and microstrain of hydroxylapatite, by Rietveld full pattern fitting. The instrumental line profile was evaluated employing a heat treated CeO_2 powder, tested to provide no detectable size or strain broadening. When assuming isotropic crystallite shapes for HAp, the fit was quite poor, suggesting a (hkl) dependent line broadening, and hence a significant anisotropy of the microstructure. The fit is much improved by using the Popa model for size and micro-strain anisotropy [28], implemented in the MAUD code as "Popa rules". The results containing the CaO percent, and the average crystallite sizes measured parallel and perpendicular to the *c* axis are presented in Table 1, together with the reliability factors of the fit.

Table 1: Results obtained by fitting the XRD data

Sample	CaO (wt%)	D $\parallel$ *c* (nm)	D $\perp$ *c* (nm)	Averaged microstrain $<\varepsilon^2>^{1/2}$	Rwp (%)
HAP-80	0	43	20	0.0019	4.34
HAP-600	0	44	20	0.0018	4.34
HAP-800	0.31 ± 0.03	97	62	0.0010	5.29
HAP-1000	1.13 ± 0.03	143	127	0.0005	5.94

It results that the HAp crystallites are elongated along the *c* crystallographic axis. As the heat treatment temperature increases above 800°C they become less elongated and larger, approaching sphere shape in the powder treated at 1000°C. The microstrain was found anisotropic too, and quite large in the powders calcined at lower temperatures. In Table 1 there are given only the microstrain values averaged over all crystallographic directions. The HAp lattice becomes more and more ordered (less strained) as the temperature increases above 800°C.

The nanosized HAp powders (HAp_80) obtained by gel dried at 80°C for 96h were post-treated at temperatures between 600 and 1000°C. Figure 2 shows the SEM photograph of the post-treated powder (600^0C, 800^0C and 1000^0C). From the graphs, it can be seen that HAp morphologies is depended of the heat treatment. The powder obtained at 80^0C (HAp_80) shows particles dispersed in form of the flake. The dispersed particles with spherical shape are observed for powders treated at1000^0C.

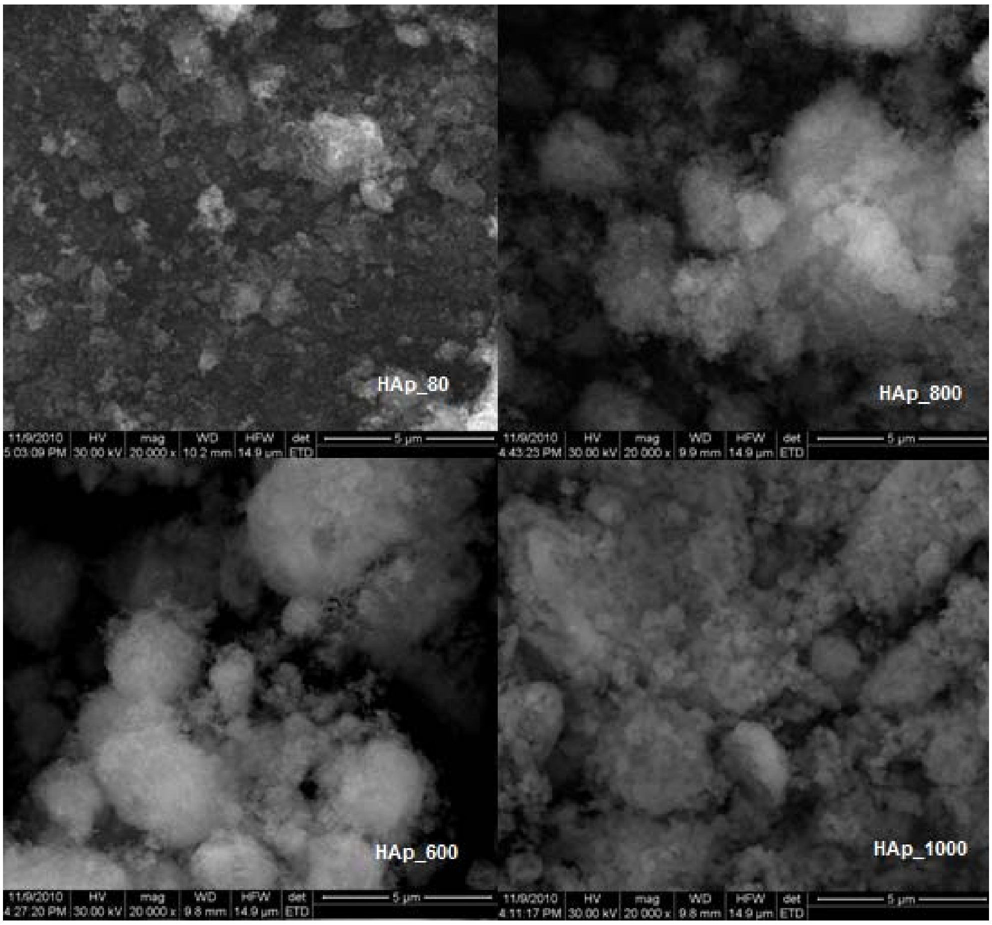

Fig. 2: Typical SEM images of the HAp_80, HAp_600, HAp_800, HAp_1000 powders.

The TEM data (Figure 3) reveal the structural evolution of the material at the different temperatures (SAD micrography) and its texture (shape and size distribution on BF micrography).

HaP	Bright Field (BF) bar = 200 nm	Selected Area Diffraction (SAD)
80°C		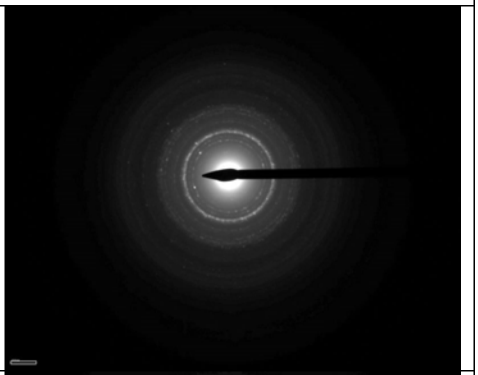
600°C		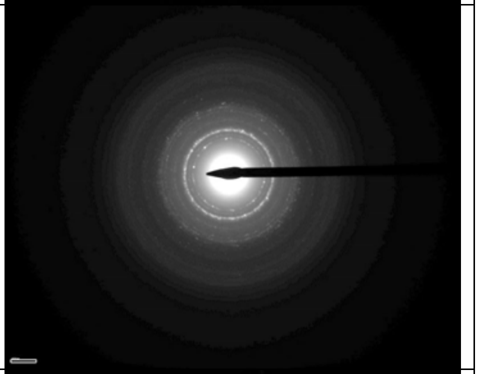
800°C	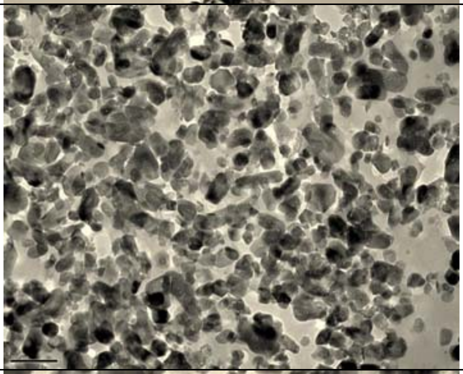	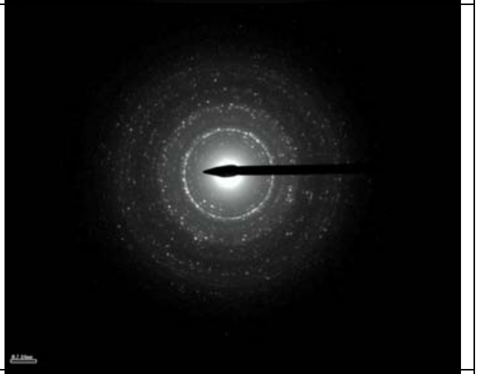
1000°C	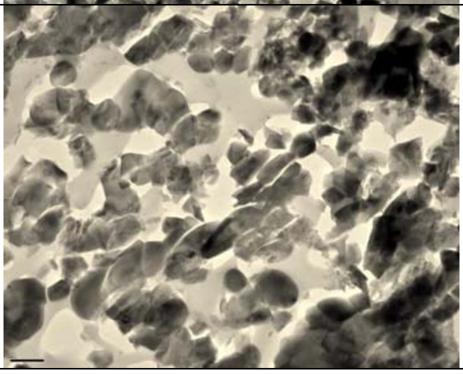	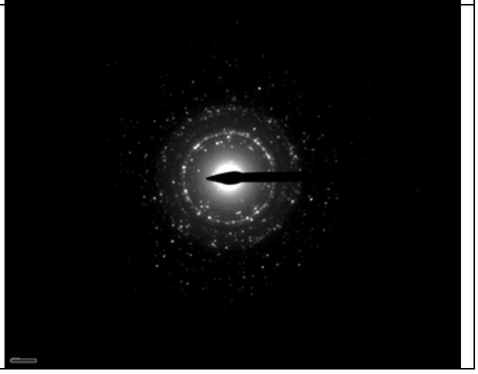

Fig. 3. Micrographs (BF and SAD) of HAp at 80°C, 600°C, 800°C and 1000°C.

At 80°C the material is crystallized (Debye-Scherer type) and composed of small crystals with a maximum size around 100 nm. At 600°C the SAD micrography exhibits more diffraction spots corresponding to larger crystals observable on the corresponding BF, with a maximum (average) size around 120 nm. Next temperature of post treatment (800°C) induces same trend with crystal growth (more dot thinner spots on the SAD micrography) and a crystal size around 180 nm). Finally at 1000°C the SAD micrography reveals a polycrystalline material perfectly ordered along the three directions of the reciprocal space corresponding to large crystal with average size around

280 nm. The average size of the different samples versus the treatment temperature (Figure 4) fit perfectly with a polynomial equation of third order.

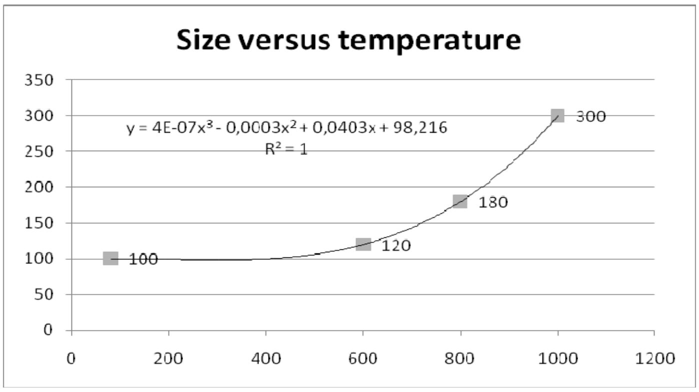

Fig. 4. Maximum (average) size of the crystals versus the treatment temperature of the samples.

The indexation of the SAD using the electron diffraction equation issued from Bragg law (1)

$$d=L\lambda/R \qquad (1)$$

d is the (hkl) distance,
L the camera length of the TEM in SAD mode,
λ corresponds to the wavelength of the electrons beam at 120 keV
R is measured on the micrography.

The Lλ corresponds to a constant of the electron microscope and has been previously calculated using reference materials (pure gold or platinum, graphite), while R is measured using specific tools from Digital Micrograph software (Gatan technologies). The SAD micrography represents a part of the reciprocal space of the material than what can be obtained by XRD. The specimen holder being a single tilt one allows restricted tilt inclination of the specimen in the TEM. For this reason only diffraction plane in Bragg condition will contribute to the diffraction pattern obtained. The distances found are reported in the Table 2. At 80°C and 600°C only calcium phosphate hydroxide (file JCPDF 9-434) has been identified. At higher temperature (800°C and 1000°C) additional phase appears. If at 800°C only one distance doesn't fit with the XRD pattern of hydroxyl apatite, 3 distances at 1000°C doesn't match with the HAp.

Table 2: The distances d (Å) calculated for HAp at 80°C, 600°C, 800°C and 1000°C.

d (Å) 80°C	hkl	d (Å) 600°C	hkl	d (Å) 800°C	hkl	d (Å) 1000°C	hkl
5,258	(101)	3,511	(201)	8,183	(100)	9,117	?
4,095	(200)	3,374	(002)	5,612	?	5,247	(101)
3,494	(002)	3,134	(102)	5,258	(101)	3,691	?
3,161	(102)	3,102	(210)	4,583	(100)	3,133	(102)
2,775	(112)	2,827	(211)	4,129	(100)	2,784	(112)
2,272	(310)	2,291	(212)	3,446	(002)	2,098	?
		1,973	(222)	3,143	(102)	1,806	(321)
		1,859	(213)	2,823	(211)		
				2,550	(301)		
				2,293	(212)		
				2,057	(113)		

Fig. 5A shows the FT-IR spectra of the HAp at 80^0C, and heated at 600^0C, 800^0C and 1000^0C. The fundamental vibration modes of PO_4^{3-}, ν_1, ν_2, ν_3 and ν_4, are observed. FTIR spectra (Figure 5B and Figure 5C) indicate that all the samples exhibit the characteristic bands of phosphate groups of the apatitic structure at about 470 cm^{-1} (ν_2), 550 and 600 cm^{-1} (ν_4), 960 cm^{-1} (ν_1) and 1020-1120 cm^{-1} (ν_3) [29-33]. The band at 1400 cm^{-1} was attributed to residual NO_3^- groups resulting from synthesis precursors. The band at 860 cm^{-1} is associated with ν_2 vibrations of carbonate groups, and at 1470 cm^{-1} is associated with ν_3 vibrations carbonate groups [34]. CO_3^{2-} and NO_3^- are the common impurities in the HAp synthesis. The intensities of both CO_3^{2-} and NO_3^- peaks decreased at higher calcinations temperatures because they are released as volatile gases (Figure 5C). The spectrum of HAp had characteristic bands at 632 and 3572 cm^{-1}, corresponding to O-H groups located in the apatite channels (Figures 5B, 5C and 5D) [35]. The pronounced hydroxyl bands at 632 and 3572 cm^{-1} are typical of hydroxyapatite with a high degree of crystallinity, powder sintered at high temperature [36]. The broad bands in the regions 1600-1700 cm^{-1} and 3200-3600 cm^{-1} correspond to H-O-H bands of lattice water [37-38]. In all the spectra of the samples heated, the intensity of the large bands which was attributable to adsorbed water is diminished (Figs. 5C and 5D).

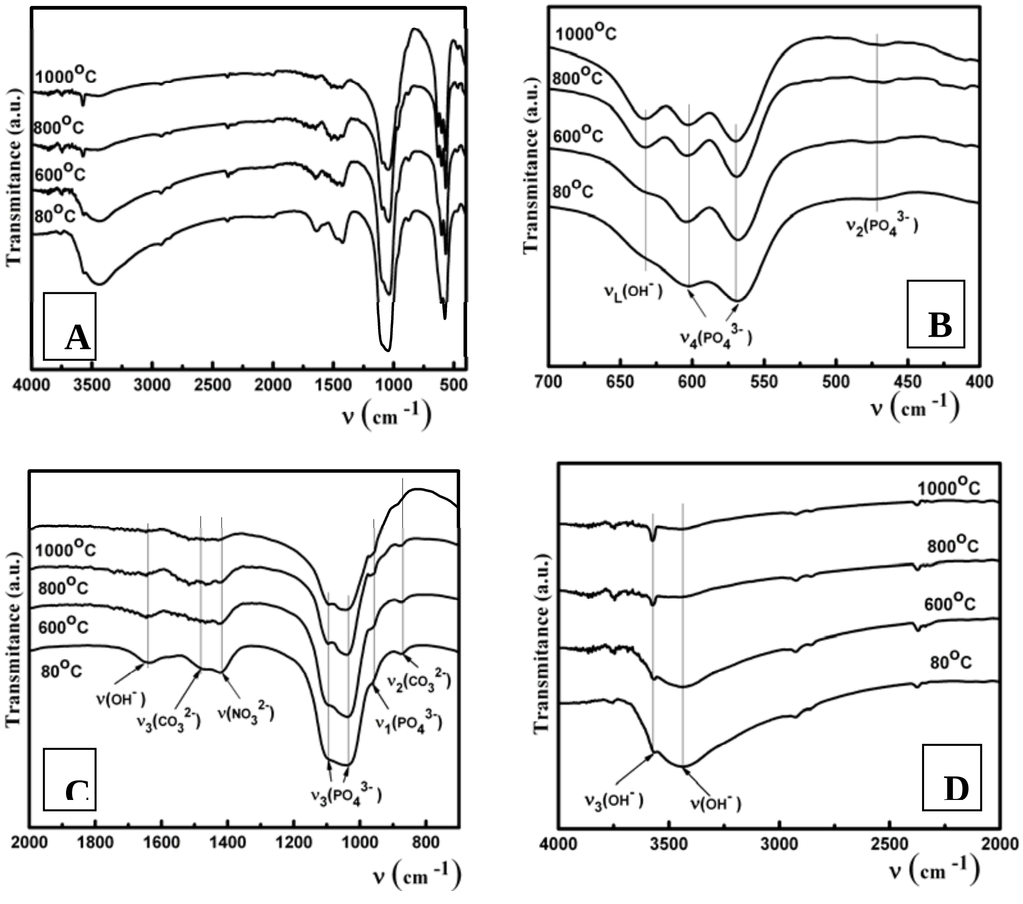

Fig. 5. The FT-IR spectra of powder HAp at 80^0C and sintered at 600^0C, 800^0C and 1000^0C.

The Raman spectra of the HAp samples are presented in the figure 6. The vibrational spectra of HAp powders exhibit a strong molecular character associated with the internal modes of the PO_4^{3-} tetrahedral ν_1 frequency (960 cm^{-1}) corresponds to the symmetric stretching of P-O bonds; ν_2 (430 cm^{-1} and 446 cm^{-1}) is attributed to the O-P-O bending modes; ν_3 (1074 cm^{-1}, 1028 cm^{-1} and 1045 cm^{-1}) corresponds to asymmetric P-O stretching and also P motion and ν_4 (578 cm^{-1}, 590 cm^{-1} and 608 cm^{-1}) can be addressed manly to O-P-O bending character.

The Raman spectra are in a good agreement with the data reported in literature [39-46]. It was observed that all the samples exhibit the very intense band characteristic of hydroxyapatite at ~ 960 cm^{-1} assigned to mode ν_1 of the PO_4^{3-} tetrahedron.

For the sample HAp_1000 are observed the bands at 331 cm^{-1} and 288 cm^{-1} attributed to the Ca (II)-OH and Ca-PO_4 bonds, respectively [47-48].

It was observed that after the calcination at 1000^{0}C (sample HAp 1000) the bands are more intense, the increase of the cristallinity could explain this results. The intensity depends directly on the sample crystallinity, so the highest degree of crystallinity of the HAp samples appears to be achieved after calcination at 1000^0 C [49].

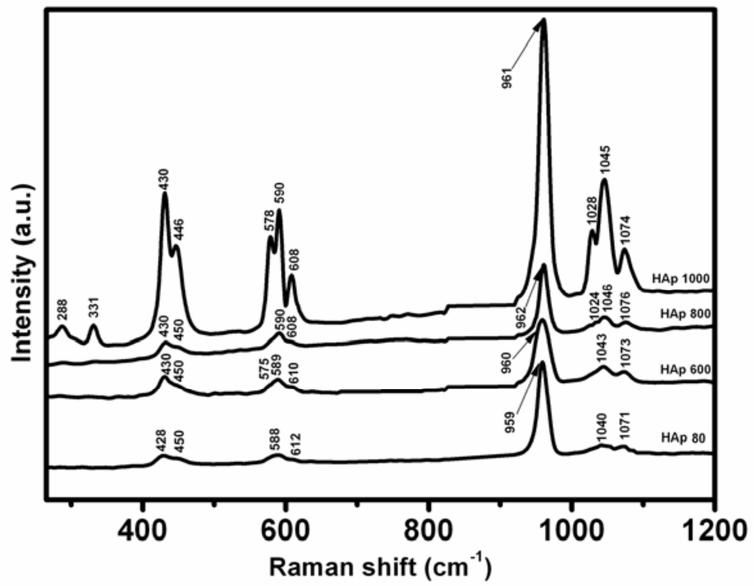

Fig. 6: Raman spectra of powder HAp at 80^{0}C and sintered at 600^{0}C, 800^{0}C and 1000^{0}C.

Fig. 7 shows the PL spectra of HAp studied at various temperatures (80, 600, 800, 1000°C).

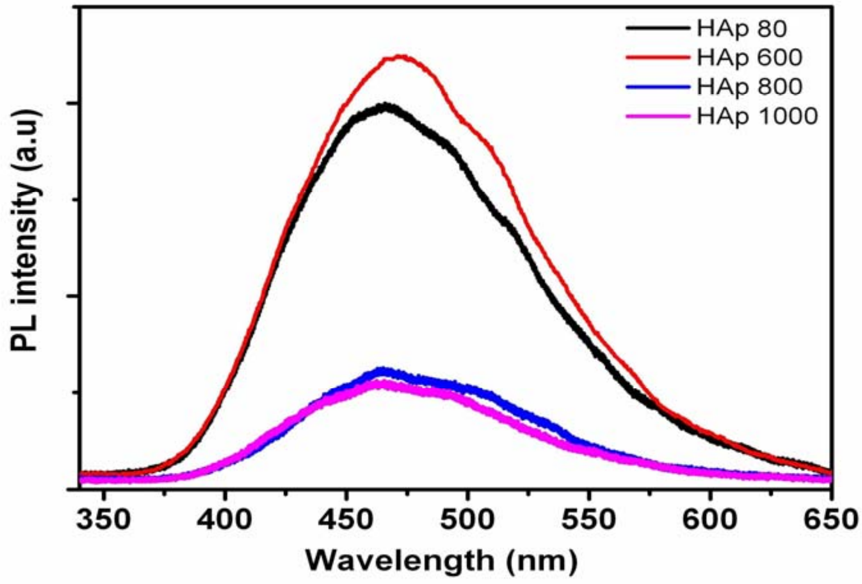

Fig. 7. PL spectra of powder HAp at 80^{0}C and sintered at 600^{0}C, 800^{0}C and 1000^{0}C

From this figure (Fig. 7), we can observe a strong emission consisting of a broadband (380–615 nm) with a maximum peaks at 465 nm for HAp _600 and HAp _80 samples, and a weak emission slightly red shift for HAp _800 and HAp_1000.

The PL decays could be fitted by considering rate equations of exciton recombination from two excited states 1 and 2 with lifetimes τ_1, and τ_2 [50]. The fitting curves, indicated as solid red lines in Figure 8 are consistent with the experimental decay curves as dotted black lines in the range 0-5 ns; lifetimes of the emission of HAp_80 are τ_1 = 0.41 ns, τ_2 =2.27 ns and for HAp_1000 are τ_1 = 0.023 ns, τ_2 = 1.1 ns. It is clear that shorter lifetimes are observed in the case of HAp_1000.

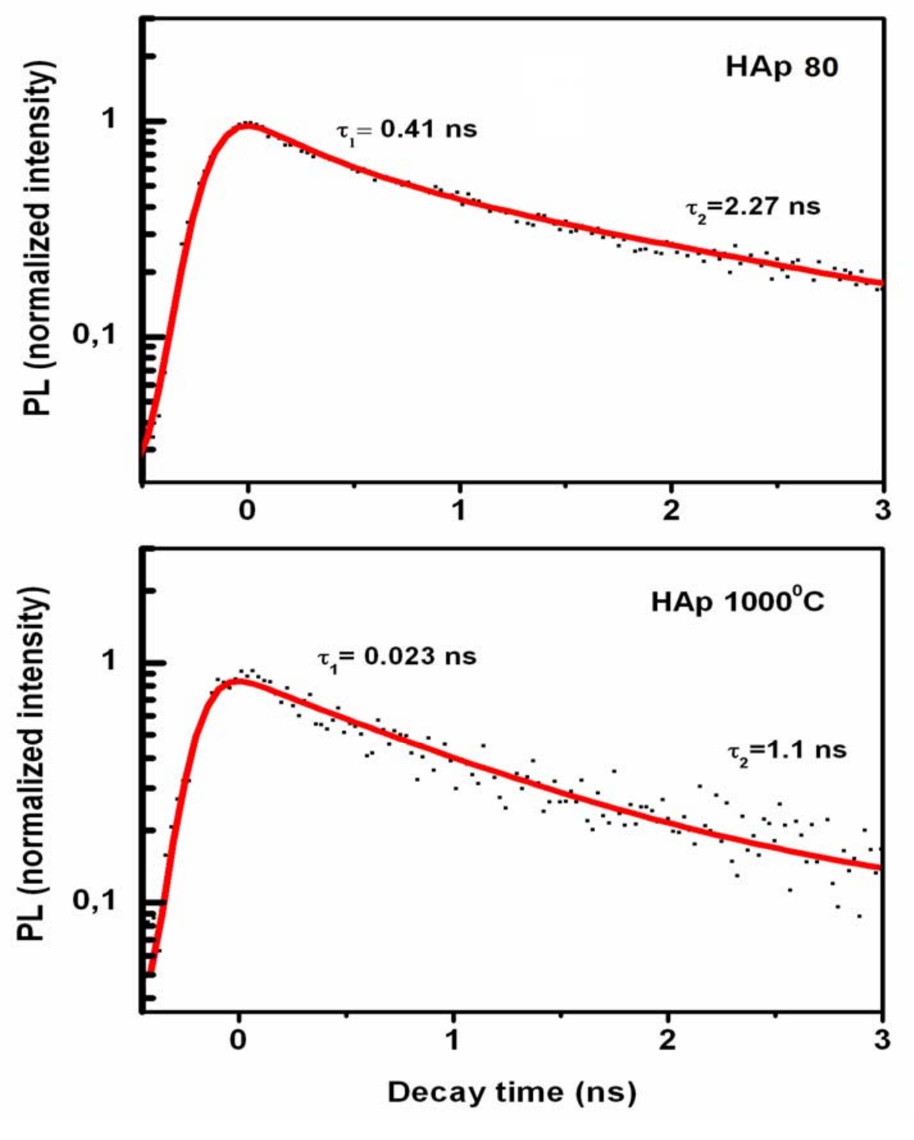

Fig. 8. Time-resolved PL decay of HAp_80 and HAp_1000. The solid-lines are the fitting line. The decay times of HAp_80 and HAp_1000 are τ_2 *= 2.27 ns and* τ_2 *= 1.1ns, respectively.*

Since neither the Ca^{2+}, nor the PO_4^{3-} are supposed to present luminescent properties, luminescence signal in our Hap samples probably comes from defects and /or impurities introduce during the synthesis in the host matrix. Zhang et al reported the same behavior for Strontium hydroxyapatite [51-52] and for Calcium hydroxyapatite [53]. They attributed this luminescence to the $CO_2^{\bullet-}$ radicals. They observed a broad luminescence band centered at 427 nm. Until now, the shift with our samples is not well understood but other group observes for Ca-Hap a broad luminescence centered at 500 nm [54]. The location of this broad band probably depends on the synthesis conditions. Furthermore, the short decay rates in the nanosecond scale well confirm the signature of a defects/impurities luminescence behavior. In our study we can observe a huge decrease of the photoluminescence intensity by increasing the temperature of the synthesis. This can be explain by the increase of the crystallite size observe in previous experiment which can decrease the number of defects/impurities in the host lattice.

Celular morphology was investigated using FESEM to obtain qualitative information of osteoblast cells on HAp samples. Fig. 9 shows representative SEM morphologies of osteoblasts hFOB 1.19 cells grown on the discs hydroxyapatite surface after 12 h. The cells on the HAp at 80^0C did not spread out over the surface, as shown in Figure 9 (HAp_80). In contrast, on the HAp sintered at 800^0C and 1000^0C the cell was found to have numerous fine filopodia attached to the surface (HAp_800 and HAp_1000). Furthermore, the cell on the HAp sintered at 1000^0C had longer filopodia than those on the HAp at 80^0C, 600^0C and 800^0C. The results demonstrate that the HAp sintered at 1000^0C promoted osteoblasts cells attachment and adhesion.

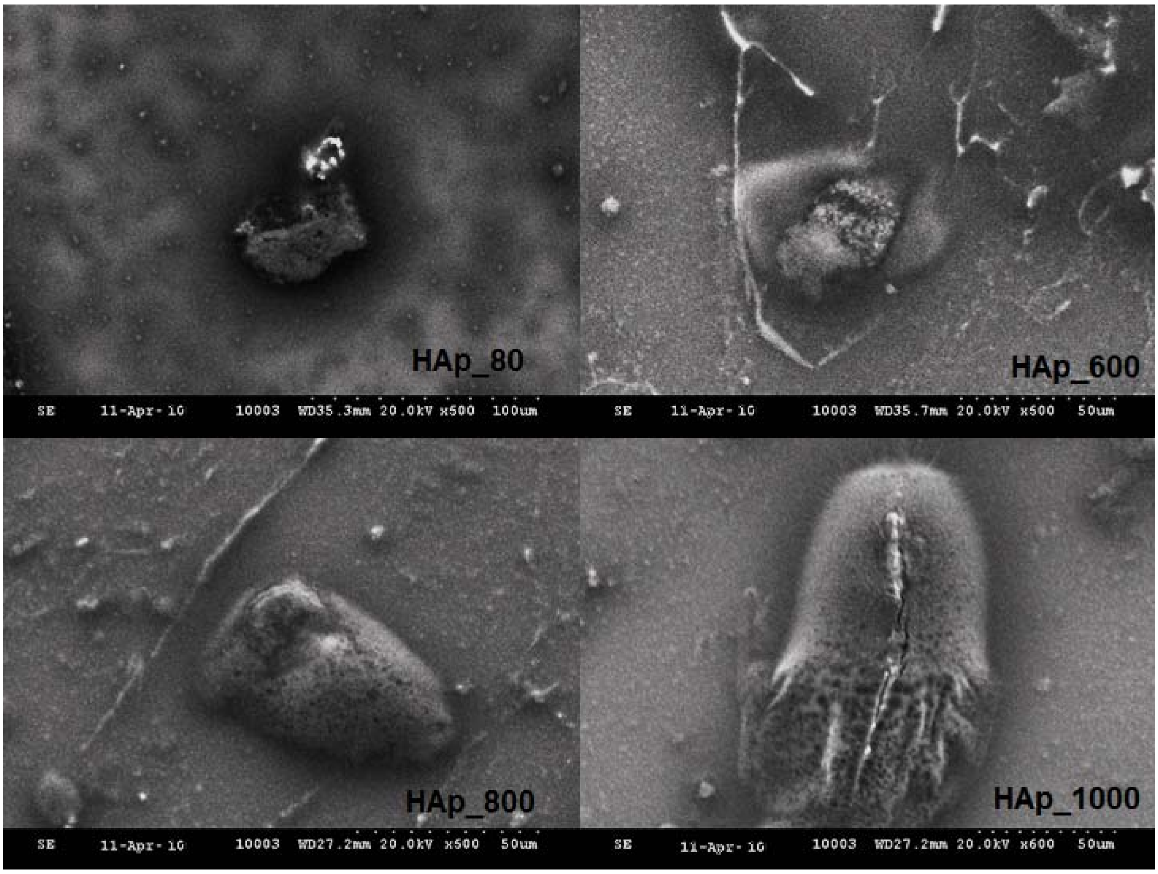

Fig. 9: FESEM micrographs of osteoblasts hFOB 1.19 cells attached to the specimens: HAp at 80^0C (HAp_80), HAp sintered at 600^0C (HAp_600), HAp sintered at 800^0C (HAp_800) and HAp sintered at 1000^0C (HAp_1000)

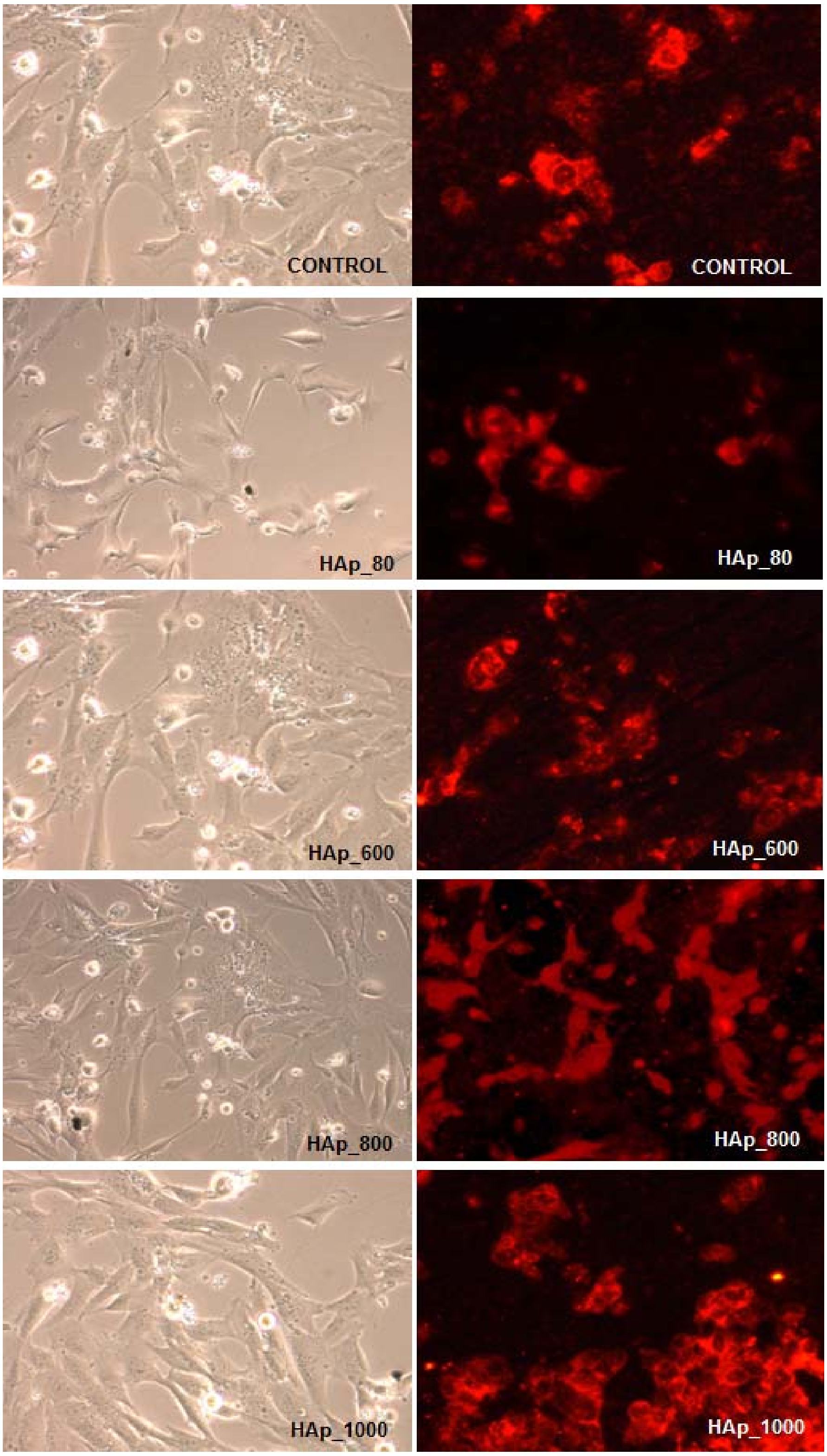

Fig. 10: Microscopical analysis of hFOB 1.19 cells plated on HAp_80, HAp_600, HAp_800 and HAp_1000 for 24 hours; cell morphology (left), hypericin staining (right).

None of the ceramics altered the cellular morphology in term of size and shape (Figure 10 - left) is observed. On the all material types, no specific orientation of the centrosome and similar extent of microtubules polymerization (Fig. 10 - right) were noticed.

As shown in Fig. 11 the osteoblasts hFOB 1.19 cells on HAp_80, HAp_600, HAp_800 and HAp_1000 proliferated with increasing culturing time (up 4 days). Furthermore, cell number was significantly higher on HAp_1000 compared to HAp_80 after 2 and 3 days of incubation, though there was no significant difference between both surfaces after 1 day of incubation. The number of hFOB 1.19 cells on control HAp_80, HAp_600, HAp_800 and HAp_1000 was 400±30, 360±25, 350±21, 320±16 and 300±10 after 3 days.

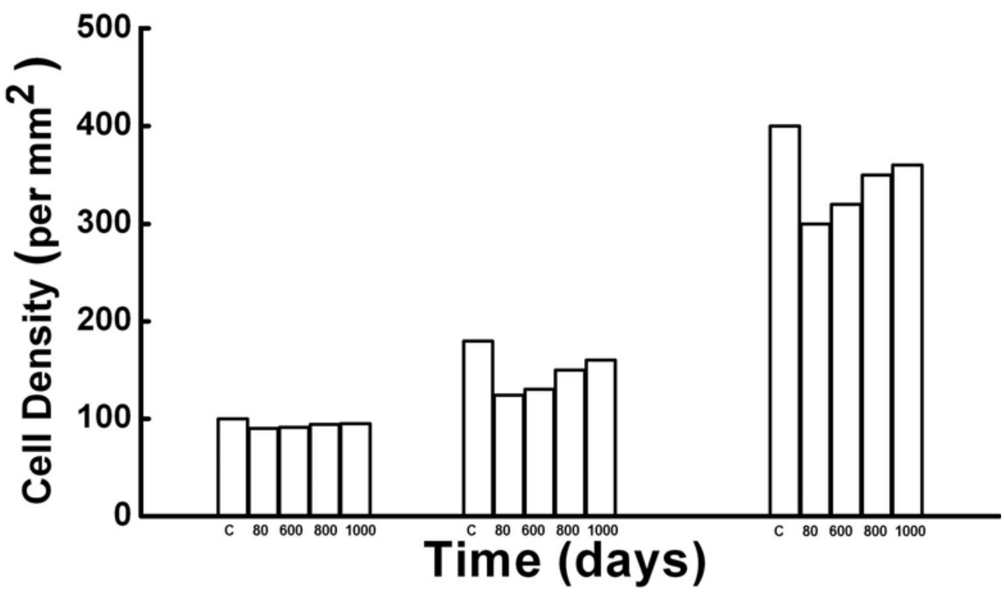

Fig. 11. The osteoblasts hFOB 1.19 cells on control (C), HAp_80 (80), HAp_600 (600), HAp_800 (800) and HAp_1000 (1000) proliferated with increasing culturing time (up 3 days).

4. Conclusions

In this study, the nano-HAp particles with controlled dimension were synthesized. The physical and chemical analyses of the HAp sintered at different temperature are considered very reliable based on the consistency of the combined results. The influence of the calcination treatment of the nano-HAp (from synthesis temperature up to 1000°C) and its influence on photoluminescence were investigated using several techniques. In this study we can observe a huge decrease of the photoluminescence intensity by increasing the temperature of the synthesis. All the experiments demonstrate that at 1000°C, the nano HAp tends to more ordered crystals. The sintering temperature has shown a significant effect on crystallite size and microstrain of powders calcined. The Popa model for size and micro-strain anisotropy used in this paper is a reliable method for crystallite size and micro-strain measurement. As the heat treatment temperature increases the HAp crystallites become less elongated and the average crystallite size and lattice ordering increases. In the agreement with the results of X-ray diffraction and TEM, the FTIR spectra of the sintered HAp show the absorption bands characteristic of hydroxyapatite.

The effect of heat treatment on osteoblasts hFOB 1.19 cells was evaluated. Our results demonstrate that cells proliferation is related to the heat treatment. HAp_1000 was the most effective and promoting cell growth. This work provides an interesting perspective of the role of nano-HAp as a potential ideal biomedical material for future clinical applications.

Acknowledgements

This work was financially supported by Science and Technology Ministry of Romania (PNCDI II 71-097/2007). The work has been funded by the Sectoral Operational Programme

Human Resources Development 2007-2013 of the Romanian Ministry of Labour, Family and Social Protection through the Financial Agreement POSDRU/6/1.5/S/19..

References

[1] I.R. Gibson, S.M. Best, W. Bonefield, J. Biomed. Mater.Res., **44**, 422-429, (1999)
[2] J.S. Bow, S.C. Liou, S.Y. Chen, Biomaterials, **25**, 3155, (2004)
[3] S.J. Kalita, A. Bhardwaj, H.A. Bhatt, Mater.Sci.Eng. **C27**, 441, (2007)
[4] L.L. Hench, J. Am, Ceram. Soc., **74**, 1487, (1991)
[5] D.G. Lange, D.C. Putter, J. Oral Implantol, **19**, 136, (1993)
[6] R. Z. LeGeros, in: H.M. Myers (Ed.), Calcium Phosphates in Oral Biology and Medicine, chap. 6, Karger, Basel, 1991, pp.154-157.
[7] R. Legeros, Clin. Mater., **14**, 65, (1993)
[8] S. I. Stupp, G.W. Ciegler, J. Biomed. Mater.Res., **26**, 169, (1992).
[9] H. Monma, Yogyo kyokai-Shi **9**, 814, (1987)
[10] K. De Groot, Biomaterials, **1**, 47, (1980)
[11] J.C. Henghebaert, Silicates Industrials, ¾, 37, (1988)
[12] J.W. Ferraro, Plastic Reconstruct Surgery, **5**, 2027, (1979)
[13] M. Yoshmura, H. Suda, K. Okmoto, J. Mater. Sci. **29**, 3399 (1994).
[14] W.J. Weng, J.L. Baptista, Biomaterials, **19,** 125 (1998).
[15] A. Lopez-Macipe, R. Rodriguez-Clemente, A. Hidolgo-Lopez, I. Arita, M.V. Garcia-Garduno, E. Rivera, V.M. Castano, J. Mater. Synth. Process. **6,** 121 (1998).
[16] D. Mo Liu, Q. Yahng, T. Troczynski, W. J. Tseng, Biomaterials, **27**, 1679, (2002)
[17] S.Okada, H. Ito, A. Nagai, J. Komotori, H. Imai, Acta Biomaterialia **6**, 591-597(2010).
[18] G. Simion, L.Pârvu, Neuron-Modeling and Simulation, Editura Academiei Române 2000
[19] G. Simion, F.Filip. Modelarea proceselor în biologie si fiziologie. Editura Universitatii Politehnica Bucuresti 1994.
[20] D.Predoi, R.A. Vatasescxu-Balcan, I. Pasuk, R. Trusca, M. Costache, J. Optoelectron. Adv. Mater., **10**(8), 2151 (2008),
[21] J. Mosmann, J Immunol Methods 65, 55-63, (1983).
[22] M.F. Hsieh, L.H. Perng, T.S. Chin, H.G. Perng, Biomaterials, 22, 2601, (2001)
[23] T.R.N. Kutty, Indian J. Chem. **11,** 695 (1973).
[24] H.C.W. Skinner, J.S.Kittelbergen, R.A. Beebe, J. Phys. Chem. **79,** 2017 (1975).
[25] J. Breme, Y. Zho, L. Groh, Biomaterials **16,** 239 (1995).
[26] N. Kivrac, A. Cuneyt Tas, J. Am. Ceram, Soc., 81(9), 2245, (1998)
[27] L. Lutterotti, S. Matthies, H.-R. Wenk, A.J. Schultz and J. Richardson, "Texture and structure analysis of deformed limestone from neutron diffraction spectra", J. Appl. Phys. **81**(2), 594 (1997).
[28] Popa N.C.- The (hkl) Dependence of Diffraction-Line Broadening Caused by Strain and Size for all Laue Groups in Rietveld Refinement, J. Appl. Cryst. **31**, 176-180 (1998).
[29] A. Costescu, I. Pasuk, F. Ungureanu, A. Dinischiotu, M. Costache, F. Huneau, S. Galaup, P. Le Coustumer, D. Predoi, Digest Journal of Nanomaterials and Biostructures, **5**, (4), 989 (2010)
[30] L. Bernard, M. Freche, J.L. Lacout, B. Biscans, Phosphorus Res. Bull. **10**, 364 (1999)
[31] K.C. Blakeslee, R.A. Condrate Sr, J. Am ceram. Soc. **54**, 559 (1971)
[32] S.J. Joris, C.H. Amberg, J. Phys. Chem. **75**, 3172 (1971)
[33] V.M. Bhatnagar, Bull.Soc. Chem. Fr., **8**, 1771 (1968)
[34] C.C. Silva, H.H.B. Rocha, F.N.A. Freire, M.R.P. Santos, K.D.A. Saboia, J.C. Goes, A.S.B. Sombra, Materials Chemistry and Physiscs **92**, 260 (2005).
[35] A. Bigi, E. Boanini, K.Rubini, J. Solid. State. Chem. **177**, 3092 (2004).
[36] Z. Hong, L.Luan, S.B. Paik, B. Deng, D.E. Ellis, J.B. Ketterson, A. Mello, J.G. Eon, J. Terra, A. Rossi, Thin Solid Films, **515**, 6773 (2007).
[37] D. Predoi, R. V. Ghita, F. Ungureanu, C. C. Negrila, R. A. Vatasescu-Balcan, M. Costache, J. Optoelectron. Adv. Mater., **9**(12), 3827 (2007).

[38]. D. Predoi, M. Barsan, E. Andronescu, R.A. Vatasescu-Balcan and M. Costache, Journal, of Optoelectronics and Advanced Materials, **9**(11), 3609 (2007).

[39]. P.N. de Aza, C. Santos, A. Pazo, S. de Aza, R. Cusco, L. Artus, Chem. Mater. **9**, 915 (1997).

[40] M. Weinlaender, J. Beumer, E.B. Kenney, P.K. Moy, F. Adar, J. Mater. Sci., Mater. Med. **3**, 397(1992)

[41] V. Sergo, O. Sbaizero, D. Clark, Biomaterials **18**, 477(1997).

[42] P.N. de Aza, C. Santos, A. Pazo, S. de Aza, R. Cusco, L. Artus, Chem. Mater. **9**, 912 (1997).

[43] D. Grossin et al. Acta Biomaterialia **6**, 577(2010).

[44] A. Antonakos et al. Biomaterials **28**, 3043 (2007).

[45] C.C. Silva et al. Journal of Physics and Chemistry of Solids **65**, 1031 (2004)

[46] M.R. Saeri et al. Materials Letters **57**, 4064 (2003)

[47] G. Penel, G. Leroy, C. Rey, B. Sombert, J.P. Huvenne, E. Bres, J. Mater. Sci., Mater. Med. **8**, 271 (1997).

[48] R. Cusco, F.Guitan. S. De Aza, L. Artus, Journal of European Ceramic Society **18**, 1301 (1998).

[49] B.O. Fowler, Inorg. Chem. **13**,194 (1974).

[50] F. Massuyeau, E. Faulques, H. Athalin, S. Lefrant, J. L. Duvail, J. Wéry, E. Mulazzi, R. Perego, J. Chem. Phys. **130**, 124 (2009).

[51] C. Zhang, C. Li, S. Huang, Z. Hou, Z. Cheng, P. Yang, C. Peng, J. Lin, **31**, 3374 (2010).

[52] C. Zhang, Z. Cheng, P. Yang, Z. Xu, C. Peng, G. Li, J. Lin, **25**, 13591 (2009).

[53] C. Zhang, J. Yang, Z. Quan, P. Yang, C. Li, Z. Hou, J. Lin, **9**, 2725 (2009).

[54] R.J. Chung, T. S. Chin, H.Y. Cheng, H.W. Wen, M.F. Hsieh, Biomolecular engineering **24**, 459 (2007).